

# Reading a Ruler in the Wild

Yimu Pan, Manas Mehta, Gwen Sincerbeaux, Jeffery A. Goldstein, Alison D. Gernand, and James Z. Wang, *Senior Member, IEEE*,

**Abstract**—Accurately converting pixel measurements into absolute real-world dimensions remains a fundamental challenge in computer vision, limiting progress in key applications such as biomedicine, forensics, nutritional analysis, and e-commerce. We introduce RulerNet, a deep learning framework that robustly infers scale “in the wild” by reformulating ruler reading as a unified keypoint detection task and representing the ruler as a set of geometric progression parameters invariant to perspective transformations. Unlike traditional methods that rely on handcrafted thresholds or rigid, ruler-specific pipelines, RulerNet directly localizes centimeter marks using a distortion-invariant annotation and training strategy, enabling strong generalization across diverse ruler types and imaging conditions while mitigating data scarcity. Additionally, we introduce a scalable synthetic data generation pipeline that combines graphics-based ruler creation with ControlNet-enhanced realism, significantly expanding training diversity and improving model performance. To further enhance robustness and inference efficiency, we propose DeepGP—a lightweight, feed-forward network that regresses geometric progression parameters from noisy ruler marks. DeepGP eliminates the need for iterative optimization during inference, enabling real-time scale estimation suitable for deployment in mobile or edge environments. Extensive experiments on our datasets demonstrate that RulerNet achieves accurate, consistent, and efficient scale estimation across challenging real-world conditions. These results underscore RulerNet’s utility as a generalizable measurement tool and its potential for integration with other vision components—such as segmentation, monocular depth estimation, and diagnostic pipelines—for automated, scale-aware analysis in practical, high-impact domains. An online live demo is provided.<sup>1</sup> Code and data will be publicly released.

**Index Terms**—Ruler reading, scale estimation, synthetic data generation, AI-assisted measurement.

Research reported in this publication was supported by the National Institute of Biomedical Imaging and Bioengineering of the National Institutes of Health (NIH) under award number R01EB030130 and the Burroughs Wellcome Fund (BWF). The content is solely the responsibility of the authors and does not necessarily represent the official views of the NIH or BWF. This work used cluster computers at the National Center for Supercomputing Applications and the Pittsburgh Supercomputing Center through an allocation from the Advanced Cyberinfrastructure Coordination Ecosystem: Services & Support (ACCESS) program, which is supported by NSF Grants Nos. 2138286, 2138307, 2137603, and 2138296.

Y. Pan, M. Mehta, and J. Z. Wang are with the Data Science and Artificial Intelligence Area, College of Information Sciences and Technology, The Pennsylvania State University, University Park, PA, 16802, USA. J. Z. Wang is also with the Huck Institutes of the Life Sciences, The Pennsylvania State University, University Park, PA, 16802, USA. Correspondence should be addressed to Y. Pan. (e-mails: ymp5078@psu.edu; sitao.zhang@psu.edu; jwang@ist.psu.edu)

G. Sincerbeaux and A. D. Gernand are with the Department of Nutritional Sciences, College of Health and Human Development, The Pennsylvania State University, University Park, PA, 16802, USA. A. D. Gernand is also with the Huck Institutes of the Life Sciences, The Pennsylvania State University, University Park, PA, 16802, USA. (e-mails: ges5491@psu.edu; adg14@psu.edu)

J. A. Goldstein is with the Department of Pathology, Feinberg School of Medicine, Northwestern University, Chicago, IL, 60611, USA. (e-mail: ja.goldstein@northwestern.edu)

<sup>1</sup>Demo URL: <https://huggingface.co/spaces/ymp5078/RulerNet-Demo>.

## I. INTRODUCTION

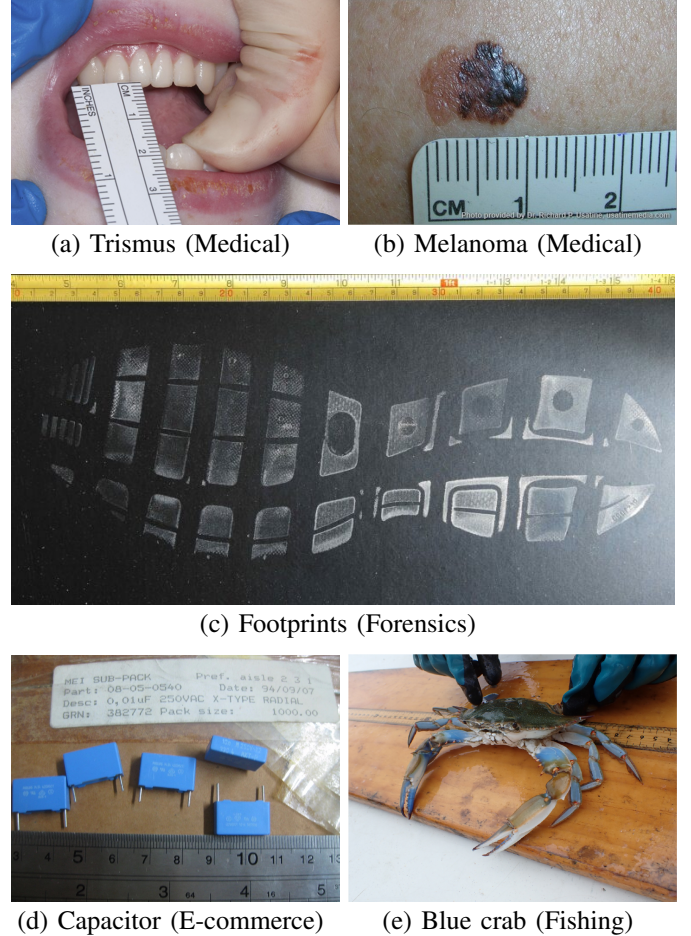


Fig. 1. Representative real-world applications where accurate ruler-based scale estimation is essential. (a) Measuring mouth opening size aids in diagnosing Trismus, a condition that restricts jaw movement [1]. (b) Determining lesion size helps identify melanoma, where size progression is a critical diagnostic cue [2]. (c) Estimating human height from footprints is a common practice in forensic analysis and crime scene reconstruction [3]. (d) Providing object size references in product images improves consumer trust and reduces returns in online shopping [4]. (e) Measuring fish length supports ecological surveys and fishery management by enabling accurate population estimates [5]. These examples highlight the broad societal relevance of accurate, automated measurement systems, motivating the need for robust, generalizable ruler reading solutions.

MODERN computer vision systems have achieved remarkable success in both low-level [6] and high-level [7] recognition tasks. A fundamental challenge persists: converting pixel measurements into absolute, real-world dimensions. This capability, known as scale estimation, is critical for scientific research and industrial applications. Accurate scale estimation bridges the gap between relative spatial patterns and precise, quantitative measurements. For instance,

in medical contexts, it supports disease diagnosis [8] and informs surgical decision [9]; in e-commerce, especially within the fashion industry, it not only simplifies the size selection process but also personalizes recommendations, leading to a more seamless shopping experience [10]–[12]; and in health and nutrition research, it facilitates accurate food weight estimation from images [13], [14]. Although deep neural networks excel at learning relative spatial patterns, they inherently lack an intrinsic understanding of metric scale, underscoring the pressing need for robust scale estimation techniques.

To overcome this limitation, practitioners often introduce reference objects [14] into scenes as metric anchors, with rulers being the most universal and accessible choice. However, deriving accurate physical dimensions from photographs using ruler-based scale calibration remains a complex challenge. Although such calibration is common in biomedical imaging [15], [16], urban planning [17]–[19], and forensics [20], [21], existing methods struggle to generalize to diverse real-world scenarios. Examples of ruler-based measures applications showing the complexity of imaging condition and diversity of rulers are shown in Fig. 1. Notably, the current state-of-the-art vision-language models (VLMs), such as ChatGPT-4o [22] with vision capabilities, are unable to correctly extract the ruler from Fig. 1, highlighting the difficulty of this task even for advanced general-purpose models. Detailed qualitative results and failure examples are provided in the appendix.

Traditional approaches rely on rigid, multi-step pipelines—ruler segmentation, intensity-based mark detection, and peak counting—that are prone to critical weaknesses:

- **Algorithmic Fragility:** Reliance on handcrafted thresholds and heuristics to detect ruler marks renders these methods vulnerable to variations in illumination, contrast, and ruler appearance—such as differences in color, texture, or mark frequency—as well as geometric distortions like perspective warping.
- **Inflexible Scale Estimation:** Estimating a single, uniform scale for an entire ruler overlooks perspective distortions. This simplification leads to significant errors, particularly when rulers are photographed at oblique angles.
- **Dataset Limitations:** Existing datasets typically include only a narrow range of ruler types, often standard metric rulers imaged under controlled conditions, due to the difficulty of collecting diverse ruler data. This leads to poor generalization to unconstrained, real-world scenarios involving unconventional rulers (e.g., minimalist printed or irregular scales, clear surfaces, glare or reflections, and white-on-black vs. black-on-white designs) and complex imaging conditions (e.g., shadows or occlusions).

**Our Approach.** We propose **RulerNet**, a unified deep learning framework that reimagines ruler reading as a geometric keypoint detection problem and achieves accurate, perspective-robust scale estimation “in the wild.” Our framework is built upon the following core innovations:

- A **distortion-invariant keypoint detection strategy** that directly localizes centimeter marks, enabling robustness

to geometric distortions and eliminating reliance on brittle ruler-specific heuristics.

- A novel **geometric progression-based scale recovery formulation**, which casts ruler reading as a constrained optimization problem in a 1D-projected space. This formulation explicitly models perspective-induced scale variation and generalizes to scenes with oblique viewpoints.
- A lightweight, feed-forward model, which regresses geometric progression parameters from noisy mark detections, enabling efficient and reliable inference even when some ruler marks are missing or spurious.
- A **scalable synthetic data generation pipeline** that combines graphics-based rendering with ControlNet-guided generative refinement, which enables training on a diverse array of ruler styles and imaging conditions without minimal annotation and address the data scarcity problem.

By addressing both algorithmic and dataset challenges, RulerNet achieves the first accurate “ruler-in-the-wild” measurement, capable of handling arbitrary ruler designs under minimal imaging constraints.

While ruler reading is itself a practically valuable task, our technical contributions extend more broadly. For instance, RulerNet can be combined with monocular depth estimation methods to recover metric depth from a single image, where the ruler serves as a physical reference to resolve scale ambiguity. In such cases, the estimated scale from RulerNet can calibrate or refine depth predictions to produce more accurate 3D reconstructions.

In the context of segmentation, RulerNet can provide per-object scale measurements once the object of interest has been segmented. This is particularly valuable in applications like medical imaging (e.g., lesion measurement), biological specimen cataloging, or inventory systems, where both localization and size are critical.

For AI-assisted diagnostics, such as detecting and measuring clinical indicators (e.g., skin lesions, wound sizes, or anatomical distances), RulerNet enables quantitative measurement directly from images without manual calibration. When integrated into diagnostic pipelines, RulerNet can enhance objectivity, reproducibility, and automation, especially in low-resource or remote settings where traditional tools may be unavailable.

Overall, RulerNet serves as a modular, interpretable component that can enrich multi-task pipelines involving detection, segmentation, and 3D understanding by grounding spatial measurements in physical units.

**Our main contributions are:**

- A deep learning reformulation of ruler reading as a geometric keypoint detection task that ensures robustness across real-world imaging conditions.
- A distortion-invariant annotation and training framework, enabling effective use of noisy or perspective-distorted ruler images.
- A fast, feed-forward geometric progression parameter regression model that supports accurate and efficient scale estimation.

- A hybrid synthetic data pipeline combining graphics-based modeling and diffusion-based realism to overcome ruler data scarcity.

## II. RELATED WORKS

### A. Ruler Detection and Reading

Object scale measurement methods [23]–[26] typically assume a standardized ruler design—uniform numbering, consistent millimeter marks, and other predictable features—even though they are not tailored to any specific application. In practice, many rulers deviate from these assumptions. Existing approaches often rely on handcrafted features, thresholding techniques on ruler mark frequencies, or object detection methods designed to identify specific patterns (e.g., digits) tailored to certain ruler types. These methods have been applied in domains including fish studies [27], forensic analysis [20], [21], [28], museum cataloging [29], urban flood monitoring and water level estimation [17], [18], [30]–[35], medical imaging [15], [16], [36]–[39], and soil profiling [19]. In contrast, our method is designed to accurately read various rulers encountered in real-world settings.

### B. Data Generation and Synthesis

Data generation and synthesis techniques are widely used to increase dataset variation and improve model performance and generalization. From an application perspective, these methods are closely related to data augmentation. Consequently, we discuss both data augmentation and generation in this section. Given the extensive literature on the topic, we focus on aspects most relevant to our application and refer readers to a comprehensive survey [40] for details.

Computer graphics-based techniques typically involve manipulating base shapes. Some approaches are implemented within visual environments [41]–[43], while others generate data directly [44]–[48] to enhance training data diversity. Generative approaches such as Generative Adversarial Networks [49]–[56] have been used to create more realistic images. More recently, diffusion models [57]–[64] have been widely utilized for generating high-fidelity, detailed images, as reviewed in [64].

Given the scarcity of ruler data, it is essential to incorporate both augmentation and data generation techniques. However, existing synthetic ruler approaches [26] have relied solely on computer graphics-based methods. In this work, we extend ruler synthesis by incorporating generative methods, bridging the gap between the two approaches.

## III. METHODS

The overall development pipeline for RulerNet is shown in Fig. 2. Each stage is described in detail in the following subsections.

### A. Ruler Detection and Reading Reformulation

Existing ruler-reading methods either target specific ruler designs or rely on frequency-based approaches. In a typical frequency-based pipeline, a ruler localization module (e.g., a

segmentation model) first isolates the ruler within the image, after which a handcrafted module analyzes the frequency of marks within the extracted region. Although deep learning-based segmentation benefits from large training data, the subsequent handcrafted mark reading step—which often assumes certain ruler appearances—remains a bottleneck for generalization.

Rather than following the traditional pipeline of addressing localization and reading separately, we reformulated the problem as a keypoint detection task that simultaneously localized and interpreted ruler marks. In practice, centimeter (cm) marks are usually visible, even when millimeter (mm) marks vary in frequency or are partially obscured. Moreover, the local regions around cm marks exhibit distinct characteristics compared to mm (which are usually shorter or thinner) or inch marks (which have a different spatial frequency). Based on these observations, by directly predicting the positions of cm marks and ignoring the rest, we eliminated the need for a separate ruler localization step and reduced dependence on ruler-specific assumptions.

We implemented this approach with a heatmap-based model [65] to predict the mark points, allowing us to integrate an off-the-shelf dense prediction model. In addition to addressing existing limitations, this keypoint strategy is inherently distortion-invariant during training: even if the image is distorted, the model can still be trained effectively using the ruler mark points. Such robustness greatly expands the available training data, which is critical given the scarcity of ruler images. Although our method is tailored for metric rulers with cm markings—owing to their wide adoption—the same data collection and training procedure can be readily adapted to imperial (inch) rulers if needed.

### B. Dataset Creation

The quantity and quality of data play a crucial role in model performance. Although natural images are abundant, ruler images are comparatively rare. To address this, we constructed a dataset that combines real and synthetic images. Additionally, we introduced a novel annotation scheme inspired by keypoint detection, which facilitates seamless integration into in-the-wild ruler reading models.

**Rulers from the Web:** We used a scripted web search to collect metric ruler images and discarded those lacking a ruler, containing only inch markings, or featuring unreadable rulers. Because our annotation process and model training had to accommodate a wide variety of ruler designs, we encountered challenges such as inconsistent mark frequencies, blurred marks, low-resolution images that obscured millimeter marks, and perspective distortions affecting local scale. To address these issues, we directly annotated the positions of ruler marks as keypoints; the ruler scale is then computed as the distance between adjacent marks. The illustration of the annotation is presented in the first column of Fig. 2, with additional samples provided in the Appendix.

**Graphics-based Synthetic Rulers:** We developed an algorithm that generates synthetic rulers superimposed on random images. Although other graphics-based methods [26] for generating ruler images exist, they are typically not open-sourced

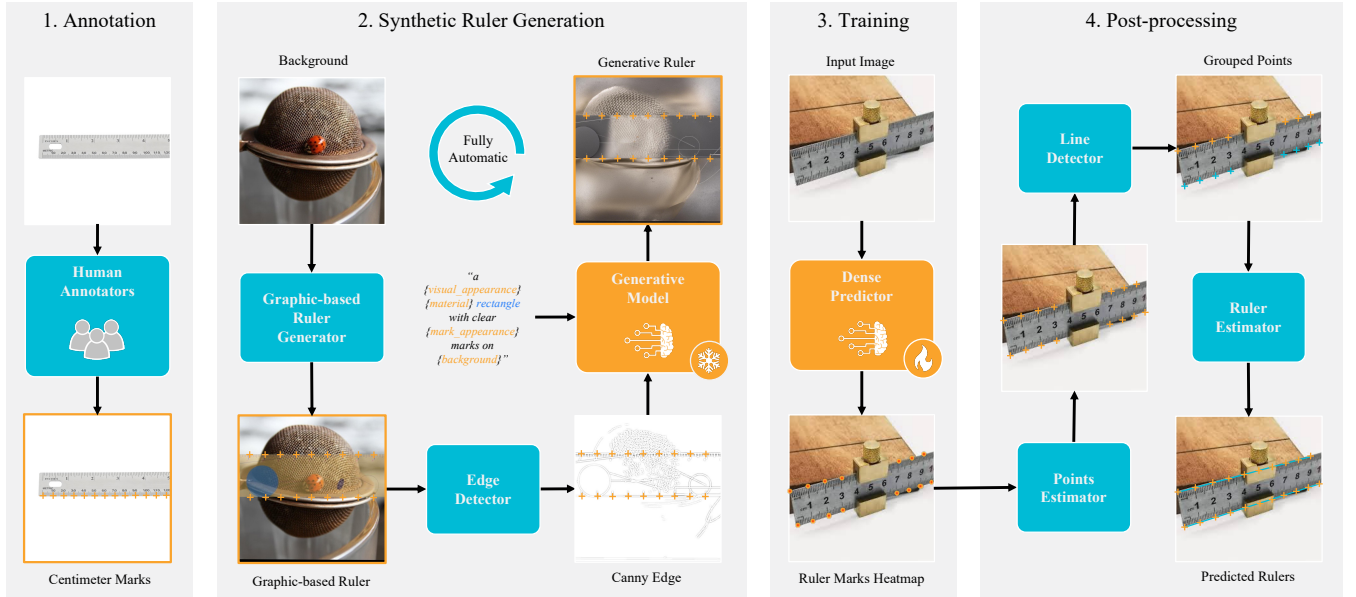


Fig. 2. Overview of the RulerNet pipeline. Annotators label centimeter marks (orange “+”) on rulers. A graphics-based generator synthesizes rulers on given backgrounds using specified parameters, followed by refinement with a frozen pre-trained generative model using its Canny edge map. A dense predictor is trained on both annotated and synthetic rulers to detect the marks, with post-processing applied to extract the final ruler (orange “+” with blue lines). Training data for the dense predictor is highlighted with an orange glow.

and fail to account for variations in ruler mark frequency, nor do they provide ground-truth ruler mark locations required for our use case.

Our objective was to create a ruler generator that facilitates training a cm mark detector, independent of the specific appearance of the ruler marks. To achieve this, we defined a set of controllable parameters that capture the range of variations observed in real-world rulers. These parameters cover multiple aspects of the generated image: for the background, we adjust the image source, perspective distortions, and random shapes; for the ruler rectangle, we control attributes such as edge color, fill color, transparency, size, edge thickness, and location; for the ruler marks, we set parameters including size, color, frequency, type (cm or inch), text font, and text placement. During training, these parameters are dynamically randomized in each iteration, with backgrounds drawn from ImageNet [66] to enhance diversity. Further details are in the Appendix.

This generator serves two main purposes: (1) it is directly integrated into the training pipeline, generating new ruler images on the fly, and (2) it acts as a foundation for the generative synthetic ruler methods described in the following subsection.

**Generative Synthetic Rulers:** Despite the advancements of graphics-based methods, there remains a significant domain gap between synthetic rulers and real-world examples. The predefined parameters used in graphics-based generation limit the variations in aspects such as illumination, material, and texture—factors that are naturally present in real images. Recently, conditional generative models like ControlNet [67] have shown remarkable success in producing realistic images and have been employed for synthetic data generation to boost model performance.

Adopting a similar strategy, we utilized a pre-trained Con-

trolNet guided by Canny edge maps for more realistic ruler generation. Our approach involved three key steps:

- Generate a synthetic ruler image using our graphics-based method.
- Extract the Canny edge map from the generated image.
- Create a descriptive prompt that captures the texture, material, and environmental details of the ruler image. The prompt, together with the Canny edge map, is used to generate a more realistic ruler image.

This hybrid approach leverages the strengths of both graphics-based generation and conditional generative modeling to bridge the domain gap and improve the realism of the synthetic data. The illustration of the data generation pipeline is presented in the second column of Fig. 2. Examples of the generated images are available in the Appendix.

### C. Model Architecture

**Ruler Mark Localization:** We formulated mark localization as a pixel-level binary classification task with probabilistic targets, represented as a heatmap. We adopted an HRNet-like [65] approach, where each mark was modeled as a 2D Gaussian centered at its location. These Gaussians were then aggregated into a heatmap, where higher probability values indicated the likely presence of ruler marks. Additionally, generating these Gaussians helped smooth out annotation inaccuracies that arose from the difficulty of precisely clicking on the ruler marks during labeling.

This formulation enables the use of any off-the-shelf dense prediction network as a keypoint detector. Formally, we train our model using a combination of Cross Entropy (CE) and DICE losses, with the latter adapted to continuous targets by squaring the source and target in the denominator. The DICE loss is defined as:



$$\mathcal{L}_{\text{DICE}}(\mathbf{X}, \mathbf{Y}) = 1 - \frac{\sum_i x_i y_i}{\sum_i x_i^2 + \sum_i y_i^2}, \quad (1)$$

where  $x_i, y_i$  are drawn from  $\mathbf{X}, \mathbf{Y}$  and  $i$  is the element index, respectively, and the total loss is given by:

$$\mathcal{L}(\mathbf{X}, \mathbf{Y}) = \lambda_{\text{CE}} \mathcal{L}_{\text{CE}}(\mathbf{X}, \mathbf{Y}) + \lambda_{\text{DICE}} \mathcal{L}_{\text{DICE}}(\mathbf{X}, \mathbf{Y}), \quad (2)$$

where  $\lambda_{\text{CE}}$  and  $\lambda_{\text{DICE}}$  are the hyperparameters.

During inference, the predicted heatmap is converted back into a point representation for scale estimation. Since the target heatmap is generated by placing 2D Gaussians around the ground-truth points, and assuming that the Gaussian parameters are chosen such that Gaussians from distinct points do not overlap (i.e., the variance is sufficiently small), mark positions can be accurately recovered by extracting the connected components or local maxima from the heatmap.

**Hough Transform for Ruler Detection:** Before scale recovery during inference, two issues must be addressed. First, an image may contain multiple rulers. Second, some points might be misclassified as ruler marks. Assuming minimal camera lens distortion during inference (i.e., non-fisheye views) and that rulers are straight, all marks belonging to a single ruler should lie along a common line—a widely accepted assumption that applies to the majority of rulers in measurement tasks. To group detected points by ruler and filter out erroneous detections, we applied a Hough transform to the detected points, grouping them based on their linear alignment. Although other RANSAC-based linear regression methods can be used, they are more difficult to be parallelized and they require more detailed hyperparameter tuning to ensure a linear relationship for each group of points.

**Scale Estimation:** Unlike prior methods [25] that assume ruler marks follow a linear progression, our approach generalizes to in-the-wild rulers by assuming only that the ruler is straight and follows a geometric progression (GP) during inference. This assumption makes our method inherently invariant to perspective distortions. Given two adjacent cm mark points,  $m_i$  and  $m_{i+1}$ , the GP can be represented as:

$$\mathcal{D}_{\text{Euclidean}}(m_{i+2}, m_{i+1}) = r \mathcal{D}_{\text{Euclidean}}(m_{i+1}, m_i), \quad (3)$$

where  $\mathcal{D}_{\text{Euclidean}}$  denotes the Euclidean distance, and  $r$  is the common ratio. When  $r = 1$ , the progression reduces to a linear scale.

To fully determine the ruler's GP, we need to estimate two initial points,  $m_0$  and  $m_1$ , and  $r$ . We formulate this as a constrained optimization problem, where the objective is to minimize the Chamfer distance between the ground-truth marks,  $\mathbf{M}_{\text{gt}}$ , and the set of points generated by  $m_0, m_1$ , and  $r$  using Eq. 3 over the range of the ground-truth points:

$$\min_{m_0, m_1, r} \mathcal{D}_{\text{Chamfer}}(\mathbf{M}_{\text{gt}}, \mathbf{M}(m_0, m_1, r)), \quad (4)$$

subject to the constraints  $r_{\min} < r < r_{\max}$  and  $\mathcal{D}_{\min} < \mathcal{D}_{\text{Euclidean}}(m_1, m_0) < \mathcal{D}_{\max}$ , where  $r_{\min}, r_{\max}, \mathcal{D}_{\min}$ , and  $\mathcal{D}_{\max}$  are hyperparameters. Here,  $\mathbf{M}(m_0, m_1, r)$  denotes the set of points generated by the GP model.

In the optimization process, the Chamfer distance—whose computational complexity is  $\mathcal{O}(dn^2)$ , where  $d$  is the point

dimension and  $n$  is the number of points—is computed repeatedly. Therefore, a more efficient computation of the Chamfer distance would greatly improve overall optimization efficiency. Although existing methods [68] reduce complexity from  $\mathcal{O}(dn^2)$  to  $\mathcal{O}(n \log n)$ , we further propose a simple technique for our case to reduce the effective dimension  $d$  to 1.

Unlike arbitrary 2D points, our detected points lie along a line (as determined by the Hough transform). By precomputing the line representation, we project all points onto this line, effectively reducing the problem to one-dimensional space. This allows us to compute the Chamfer distance in  $\mathcal{O}(n^2)$  or  $\mathcal{O}(n \log n)$  time, depending on the algorithm used.

To obtain the parameters  $m_0, m_1$ , and  $r$  that best represent the ruler, we employ differential evolution [69], a global optimization technique, as a baseline method to perform this optimization.

Using the GP representation of the ruler, we can compute the length of any line segment along the ruler without requiring an undistorted camera view, making our method significantly more generalizable than prior approaches. When marks are partially occluded, the model can still detect adjacent points to recover the ruler via GP extrapolation. This is advantageous in real-world scenarios, where rulers are rarely imaged in perfect alignment with the camera.

**Robustness Improvement and Inference Acceleration:** Although the GP representation significantly improves generalization, the per-sample optimization method using Chamfer distance as the objective function presents two key challenges. First, it is sensitive to noise in the detected ruler marks, such as missing or incorrectly detected points. Second, iterative optimization at inference time is computationally expensive.

To address both challenges, we introduce a novel learned inverse mapping that regresses GP parameters directly from noisy ruler mark detections. Unlike traditional GP fitting methods, our approach enables real-time metric scale estimation without iterative optimization, while remaining resilient to missing or spurious marks. This formulation is both architecture-agnostic and transferable to other 1D-structure detection tasks, such as identifying repeating elements or interval-based layouts under perspective distortion. We refer to this approach as deep learning-based geometric progression parameter estimation from points (**DeepGP**). Formally, we define:

$$m_0, m_1, r = \text{DeepGP}(\mathbf{M}_{\text{noisy}}), \quad (5)$$

where  $\mathbf{M}_{\text{noisy}}$  represents the noisy set of detected ruler marks. Since the model is feed-forward, a sufficiently efficient architecture enables fast inference.

To train a robust DeepGP model, a large number of training samples are required. Fortunately, generating synthetic training data is straightforward: we randomly sample GP parameters  $m_0, m_1, r$  and construct the corresponding points using a geometric progression, as described in Algorithm 1. To simulate realistic noise in mark localization, we introduce randomness into the generated points. Because the mapping  $\mathbf{M}_{m_0, m_1, r}$  produces a list of ruler marks for any given GP configuration, sampling sufficient parameter combinations allows us to cover

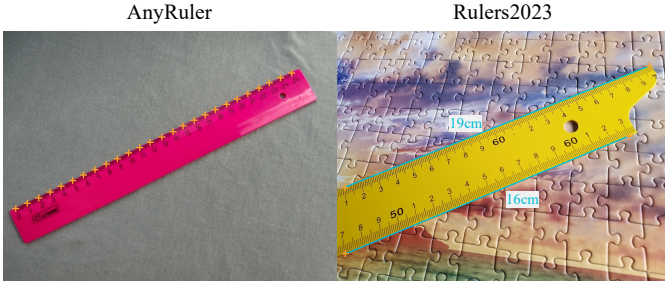


Fig. 3. Example annotations from the AnyRuler and Rulers2023 datasets. Orange '+' markers indicate point annotations, while blue lines represent line annotations, with their corresponding lengths displayed alongside them.

a wide range of plausible scenarios. Finally, since the ruler marks are constrained to lie along a straight line, we project the 2D points to 1D space before applying DeepGP, reducing computational cost while preserving geometric consistency.

---

**Algorithm 1** Generate Noisy Geometric Progression Points

---

**Require:**  $m_0, m_1$ , geometric ratio  $r$ , number of points  $n$

**Ensure:** Noisy geometric sequence  $M_{\text{noisy}}$

- 1: Initialize  $M = []$
  - 2: Set  $m_2 \leftarrow r(m_1 - m_0) + m_0$
  - 3: Append  $m_0$  and  $m_1$  to  $M$
  - 4: **for**  $i = 2$  to  $n - 1$  **do**
  - 5:    $m_i \leftarrow r(m_{i-1} - m_{i-2}) + m_{i-1}$
  - 6:   Append  $m_i$  to  $M$
  - 7: **end for** ▷  $M$  now contains  $M_{m_0, m_1, r}$
  - 8:  $M \leftarrow \{m_i + \epsilon_i \mid \epsilon_i \sim \mathcal{N}(0, \sigma^2)\}$  ▷ Add random displacements
  - 9: Remove random subset of points from  $M$
  - 10: Add random number of new random points to  $M$
  - 11: **return**  $M_{\text{noisy}} \leftarrow M$
- 

## IV. RESULTS

### A. Training and Testing Sets

We obtained 1,416 annotated ruler images with diverse appearances from the internet, collectively referred to as the AnyRuler dataset. Approximately 80% of these images were randomly selected for training, with the remaining 20% reserved for testing. In addition to evaluating performance on a variety of rulers collected from the internet, we also aimed to assess its generalizability to practical application scenarios. We used the Rulers2023 dataset [26], which contains ruler images captured under diverse conditions that differ significantly from those in the training dataset. Since this dataset was used solely for evaluation, we manually drew lines covering the cm marks and labeled the length of each line in the Rulers2023 test set, resulting in 654 images. Each sample was annotated by one annotator and verified by another. Example annotations are shown in Fig. 3.

For consistency in comparison, we extracted the pixels/cm value from each image. For the AnyRuler testing set, where labels consisted of points on visible cm marks, we first

computed the pixels/cm for all adjacent marks along the same ruler. We then took the median pixels/cm for each set of cm marks to reduce noise from missing marks. Finally, we assigned the pixels/cm value of the largest set of marks as the representative value for the image. For the Rulers2023 dataset, since we directly labeled the length of the line along the cm marks, we computed the pixels/cm for each ruler and used the value of the longest ruler for each image.

### B. Metric

We measured the difference between the prediction and the ground truth scale. Mean Absolute Pixel Error per cm (mAPE/cm) was utilized as the metric, where lower values indicated better performance. Since mAPE/cm could be affected by the ground-truth pixels/cm, we scaled it according to the image resolution to ensure a fair comparison. Specifically, we defined  $n$  as the base resolution and scaled the metric by the ratio of the current image resolution to  $n$ , termed mAPE/cm@ $n$ . Formally, it was defined as:

$$\text{mAPE/cm}@n = \frac{1}{|Q|} \sum_i \frac{n \|p_i - q_i\|}{s_i}, \quad (6)$$

where  $p_i \in \mathbf{P}$ ,  $q_i \in \mathbf{Q}$ , and  $s_i \in \mathbf{S}$  represented the predicted scales, ground-truth scales, and image sizes for the  $i$ th image in the dataset, respectively. mAPE/cm@768 was used for all experiments unless specified otherwise. Since the numbers were reported on the same dataset across different methods, the scale of each cm did not impact the evaluation.

An algorithm could either detect an incorrect scale or fail to detect the scale altogether. The former had a more negative effect, particularly when the detection was significantly off. Therefore, if the algorithm failed to detect the scale, we always set the detected scale to 0 pixels/cm.

For inference speed evaluation, we report the average number of milliseconds per sample (ms/s) across the entire dataset, excluding the first 10% of samples to eliminate the effects of loading and caching overhead. To isolate the computational cost of ruler extraction specifically, we compare only the ruler extraction modules in the ablation study.

While our primary evaluation focuses on pixels/cm conversion accuracy, we acknowledge that this assumes coplanarity between the ruler and object. This evaluation choice reflects the current absence of publicly available datasets with full 3D annotations or camera intrinsics necessary for metric calibration through homography or depth estimation. Nevertheless, our AnyRuler dataset and Rulers2023 annotations—comprising a diverse range of ruler types, imaging conditions, and annotations—represent the most comprehensive public benchmark for ruler-based scale estimation to date. We believe our work lays the foundation for future research that integrates monocular depth prediction, homography estimation, or 3D-aware measurement models.

### C. Implementation Details

**Training Setup:** The RulerNet model was both pre-trained and trained on the entire AnyRuler training set, supplemented with synthetic rulers generated from both graphics-based and

generative pipelines. The DeepGP module was implemented as a custom 1D U-Net with only 1.6M parameters and was trained on 1.23 billion randomly generated samples using a batch size of 1024 to ensure broad coverage of geometric progression scenarios. We capped the number of ruler marks at 64, as higher counts (e.g., rulers longer than 6.4 meters) result in centimeter intervals that are too small to be reliably distinguished. To standardize input for DeepGP, all mark locations were min-max normalized to the range  $[-1, 1]$ .

Since no open-source implementations were available for existing ruler reading methods, we selected two representative baselines for comparison: a digit detection-based method [25] and a mark frequency-based method [21]. The digit detection-based method was implemented using an off-the-shelf OCR model (EasyOCR<sup>2</sup>), and we incorporated localization and post-processing of the detected digit positions using our GP method to enable fair comparison. For the mark frequency-based method [21], we obtained performance results directly from the original authors; however, inference time was not available.

All experiments were conducted using Python 3.9, PyTorch 2.0.1, scikit-learn 1.5.2, OpenCV 4.8.1, and NumPy 1.26.4. All RulerNet training was performed using consistent training settings on a single NVIDIA A40 GPU, except for pre-training, which was conducted for 80 epochs on four NVIDIA A40 GPUs at a base learning rate of 0.0005. All other models were trained for 200 epochs using the AdamW optimizer with default PyTorch settings and a cosine annealing learning rate scheduler, including a 10% linear warmup phase at a base learning rate of 0.0002.

**Inference Setup:** All inference-time evaluations were performed on a cloud server equipped with an NVIDIA V100 GPU and an Intel Xeon Gold 6248 CPU.

---

#### Algorithm 2 Extract Peak Points from Heatmap (PyTorch)

---

**Require:** Heatmap  $H \in \mathbb{R}^{H \times W}$ , threshold  $\tau$ , kernel size  $k$ , Gaussian  $\sigma$

**Ensure:** Coordinates  $C$  of peak points

```

1:  $K \leftarrow$  predefined Gaussian kernel with  $\sigma$ 
2:  $S \leftarrow \text{conv2d}(H, K, \text{padding} = k/2)$ 
    $\triangleright$  Compute X-direction local maxima
3:  $dx \leftarrow \text{diff}(S, \text{dim} = 1)$ 
4:  $x_{\text{left}} \leftarrow (dx[:, :, -1] > 0)$ 
5:  $x_{\text{right}} \leftarrow (dx[:, :, 1] < 0)$ 
6:  $x_{\text{peaks}} \leftarrow \text{pad}(x_{\text{left}} \wedge x_{\text{right}}, \text{pad} = (1, 1))$ 
    $\triangleright$  Compute Y-direction local maxima
7:  $dy \leftarrow \text{diff}(S, \text{dim} = 0)$ 
8:  $y_{\text{top}} \leftarrow (dy[:, -1, :] > 0)$ 
9:  $y_{\text{bottom}} \leftarrow (dy[:, 1, :] < 0)$ 
10:  $y_{\text{peaks}} \leftarrow \text{pad}(y_{\text{top}} \wedge y_{\text{bottom}}, \text{pad} = (1, 1))$ 
    $\triangleright$  Find valid peaks above threshold
11:  $P \leftarrow x_{\text{peaks}} \wedge y_{\text{peaks}} \wedge (S > \tau)$ 
12:  $C \leftarrow \text{nonzero}(P)$ 
13: return  $C$ 

```

---



---

#### Algorithm 3 Hough Line Detection (PyTorch)

---

**Require:** Point set  $P \in \mathbb{R}^{N \times 2}$ , angle step  $\Delta\theta$ , resolution  $\Delta\rho$

**Ensure:** Points  $P_{\text{max}}$  supporting the dominant line

```

    $\triangleright$  Generate angle and rho candidates
1:  $\Theta \leftarrow \text{deg2rad}(\text{arange}(-90, 90, \Delta\theta))$ 
2:  $X, Y \leftarrow P[:, 0], P[:, 1]$ 
3:  $\rho \leftarrow X \cos(\Theta) + Y \sin(\Theta)$ 
    $\triangleright$  Compute all  $\rho_{i,j}$ 
4:  $\rho_{\text{max}} \leftarrow \text{ceil}(\max(\text{norm}(P, \text{dim} = 1)))$ 
5:  $B_{\rho} \leftarrow \text{arange}(-\rho_{\text{max}}, \rho_{\text{max}} + \Delta\rho, \Delta\rho)$ 
6:  $\rho_{\text{idx}} \leftarrow \text{bucketize}(\rho, B_{\rho})$ 
    $\triangleright$  Vote in the accumulator
7:  $A \leftarrow \text{zeros}(\text{len}(B_{\rho}), \text{len}(\Theta))$ 
8:  $\text{scatter\_votes}(A, \rho_{\text{idx}}, \Theta)$ 
    $\triangleright$  Smooth the accumulator
9:  $K \leftarrow$  predefined kernel
10:  $A \leftarrow \text{conv2d}(A, K, \text{padding} = 1)$ 
    $\triangleright$  Detect peaks in the accumulator
11:  $M \leftarrow A > 0.3 \cdot \max(A)$ 
12:  $(i_r, i_{\theta}) \leftarrow \text{nonzero}(M)$ 
13:  $R, T \leftarrow B_{\rho}[i_r], \Theta[i_{\theta}]$ 
    $\triangleright$  Assign points to each detected line
14:  $D \leftarrow |R - (X \cos T + Y \sin T)|$ 
15:  $M_{\text{assign}} \leftarrow D < \Delta\rho$ 
16:  $C \leftarrow \text{sum}(M_{\text{assign}}, \text{dim} = 1)$ 
    $\triangleright$  Return points from the line with most support
17:  $k^* \leftarrow \text{argmax}(C)$ 
18:  $P_{\text{max}} \leftarrow P[M_{\text{assign}}[k^*]]$ 
19: return  $P_{\text{max}}$ 

```

---

**Post-processing:** We extract ruler marks from the predicted heatmap using a custom PyTorch implementation of a local maxima detection approach, as detailed in Algorithm 2. Hough line detection is also implemented in PyTorch and operates directly on the detected points, as shown in Algorithm 3. For Chamfer distance computation, we use a brute-force implementation with  $\mathcal{O}(n^2)$  complexity. Differential evolution is implemented using scikit-learn’s optimizer with the `randlbin` strategy and Latin hypercube initialization.

The bounds for optimization are set as  $r_{\text{max}} = 1.5$ ,  $r_{\text{min}} = \frac{1}{1.5}$ ,  $\mathcal{D}_{\text{max}} = \max(\mathbf{D}_{\text{direct}})$ , and  $\mathcal{D}_{\text{min}} = \min(\mathbf{D}_{\text{direct}})$ , where  $\mathbf{D}_{\text{direct}}$  is the set of distances between adjacent detected points. For DeepGP, no bounds are required, and all input mark locations are min-max normalized to the range  $[-1, 1]$ .

**Graphics-based Image Generator Parameters:** The parameters for the graphics-based ruler generator are listed in the Python-like function call in Listing 1. We used a script to randomly generate these parameters when generating ruler images.

**Available Values for the ControlNet Prompt Variables:** We used ChatGPT to generate a set of possible values for each variable in the ControlNet [67] prompt “a {visual\_appearance} {material} rectangle with clear {mark\_appearance} marks on {background}.” The available values for each variable are listed in Table I and were randomly sampled when generating ruler images.

<sup>2</sup><https://github.com/JaidedAI/EasyOCR>

**Listing 1** Python-like function to draw a ruler with various customization parameters.

```

1 draw_ruler(
2     # Basic parameters
3     image, # The image canvas on which the ruler will be drawn.
4     position, # The starting (x, y) coordinates for drawing the ruler.
5     length_cm, # The total length of the ruler in centimeters.
6     cm_to_px=37.7952755906, # Conversion factor to convert centimeters to pixels.
7     ruler_height_cm=3, # Height of the ruler (in cm) as it appears on the image.
8     ruler_extension_fraction=0.2, # Fraction of the ruler length to extend beyond the ruler mark
9     ↪ area.
10    orientation="horizontal", # Orientation of the ruler: "horizontal" or "vertical".
11
12    # Style parameters
13    fill_color=(255, 255, 255), # RGB color tuple used to fill the ruler's background.
14    edge_color=(0, 0, 0), # RGB color tuple for drawing the ruler's edges.
15    thickness=2, # Thickness (in pixels) of the ruler's border/outline.
16    alpha=0.5, # Transparency level of the ruler (0 = fully transparent, 1 = fully opaque).
17
18    # Mark interval parameters
19    mm_mark_interval=1, # Distance (in millimeters) between successive mm marks.
20    inch_mark_interval="1/16", # Interval between inch marks, expressed as a fraction of an inch.
21
22    # Font parameters for cm and inch labels
23    cm_font=cv2.FONT_HERSHEY_SIMPLEX, # Font type for centimeter labels.
24    inch_font=cv2.FONT_HERSHEY_SIMPLEX, # Font type for inch labels.
25    cm_font_scale=0.5, # Scaling factor for the centimeter label font size.
26    inch_font_scale=0.5, # Scaling factor for the inch label font size.
27    cm_font_color=(0, 0, 0), # RGB color tuple for the centimeter label text.
28    inch_font_color=(0, 0, 0), # RGB color tuple for the inch label text.
29    cm_font_offset_x=0, # Horizontal offset for positioning centimeter labels.
30    cm_font_offset_y=0, # Vertical offset for positioning centimeter labels.
31    inch_font_offset_x=0, # Horizontal offset for positioning inch labels.
32    inch_font_offset_y=0, # Vertical offset for positioning inch labels.
33
34    # Mark length parameters
35    cm_mark_length=20, # Length (in pixels) of the main centimeter marks.
36    mm_mark_length=10, # Length (in pixels) of the millimeter marks.
37    half_cm_mark_length=15, # Length (in pixels) of the half-centimeter marks.
38    inch_mark_length=20, # Length (in pixels) of the main inch marks.
39    sub_inch_mark_length=10, # Length (in pixels) for smaller divisions of an inch.
40    half_inch_mark_length=15, # Length (in pixels) of the half-inch marks.
41
42    # Mark color parameters
43    cm_mark_color=(50, 50, 50), # RGB color tuple for centimeter marks.
44    mm_mark_color=(50, 50, 50), # RGB color tuple for millimeter marks.
45    inch_mark_color=(100, 100, 100), # RGB color tuple for inch marks.
46    sub_inch_mark_color=(100, 100, 100), # RGB color tuple for sub-inch marks.
47
48    # Label display options
49    show_cm_numbers=True, # Boolean flag to display numeric labels for centimeters.
50    show_inch_numbers=True, # Boolean flag to display numeric labels for inches.
51
52    # Perspective transform parameters
53    tilt_factor_horizontal=0.1, # Factor controlling horizontal tilt for a perspective effect.
54    tilt_factor_vertical=0.1, # Factor controlling vertical tilt for a perspective effect.
55
56    # Random shape parameters
57    num_random_lines=10, # Number of random lines to add for decorative effects.
58    num_random_shapes=10, # Number of random shapes to add for decorative effects.
59
60    # Additional side marks
61    other_marks="none", # Option to add extra side marks; choices: "none", "cm", "inch".
62    mark_offset=0, # Offset (in pixels) for positioning extra marks from the ruler edges.
63    draw_cm_line=False, # Boolean flag to draw a continuous line along the centimeter marks.
64    cm_line_color=(0, 255, 0), # RGB color tuple for the line drawn along centimeter marks.
65    cm_line_thickness=2 # Thickness (in pixels) of the line drawn along centimeter marks.
66 )

```

## D. Comparison with Existing Methods

Our final RulerNet (RulerNet-DeepGP) was implemented using a MobileNetV4 [70] with a UNet [71] architecture at a resolution of  $768 \times 768$  for the dense predictor, and the DeepGP model for ruler extraction.

Although previous methods have demonstrated strong performance in specific domains, Table II shows that RulerNet is the only method capable of reliably performing ruler reading across a diverse range of images, achieving a pixel error of less than 1.5 pixels per centimeter. In contrast, existing approaches fail to generalize effectively in unconstrained settings. These

results reinforce our motivation for the design of RulerNet and validate its robustness across real-world scenarios. Furthermore, RulerNet-DeepGP offers a favorable improvement for both accuracy and efficiency, enabling real-time ruler reading. Our final implementation is able to extract the ruler—i.e., the geometric progression parameters—in an end-to-end fashion and is lightweight enough to be deployed on edge devices.

From Fig. 4, we observe that RulerNet handles challenging cases, such as when the mark color is similar to the ruler color or when there is significant perspective distortion. The larger error in the third column arises from averaging the



TABLE I  
AVAILABLE PROMPT VARIABLE VALUES.

material	visual_appearance	mark_appearance	background
plastic	reflective	engraved	a wooden desk
wood	transparent	printed	white paper
metal	opaque	embossed	a blackboard
glass	matte	debossed	metal surface
rubber	glossy	stamped	a glass table
composite materials	textured	laser-etched	concrete floor
paper	smooth	painted	a marble countertop
cardboard	colored	raised	fabric surface
	patterned	indented	a grass field
	gradient	dotted	sandy surface
	frosted	striped	a water surface
	clear	highlighted	carpet
		faded	tile floor
		bold	a painted wall
		thin	a digital screen
		dual-color	a chalkboard
		metallic	cardboard sheet
		contrasted	a leather surface
		glowing	a plastic sheet
		reflective	the sky background
			a blurred background
			none

TABLE II  
PERFORMANCE COMPARISON WITH EXISTING METHODS (MAPE/CM@768). RULERNET WAS EVALUATED AT A RESOLUTION OF  $768 \times 768$ , WHILE THE DIGITS DETECTION METHOD WAS IMPLEMENTED BY US AND EVALUATED AT THE ORIGINAL RESOLUTION. THE MARK FREQUENCY METHOD WAS EVALUATED BY THE ORIGINAL AUTHORS AT OUR REQUEST. BOTH THE MEAN PERFORMANCE AND STANDARD DEVIATION ARE REPORTED (MEAN $\pm$ SD). FOR THE INFERENCE TIME, MILLISECONDS PER SIMPLE (MS/S) IS COMPUTED AS THE TIME IT TAKES FOR THE METHOD TO EXTRACT THE SCALE FROM THE IMAGE ON ANYRULER DATASET.

	AnyRuler	Rulers2023 [26]	ms/s
Digits Detection [25]	56.71 $\pm$ 92.23	76.05 $\pm$ 95.27	1530.62
Mark Frequency [21]	62.11 $\pm$ 134.41	14.79 $\pm$ 25.71	-
<b>RulerNet-GP</b>	1.32 $\pm$ 14.75	1.46 $\pm$ 4.82	2516.87
<b>RulerNet-DeepGP</b>	<b>1.19<math>\pm</math>5.03</b>	<b>1.31<math>\pm</math>3.15</b>	<b>42.18</b>

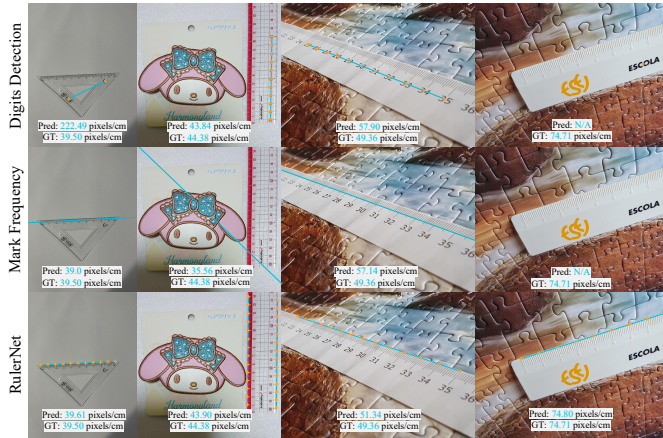


Fig. 4. Qualitative examples from the AnyRuler and Rulers2023 datasets, showing ruler localization and the final mean pixels/cm estimation. Note that the Mark Frequency method does not detect individual marks but instead identifies a line along the marks and computes a single frequency value; therefore, the orange '+' markers are absent.

pixels/cm across all cm segments in a distorted image, despite

the detected marks themselves being highly accurate on all the images. In contrast, the Digits Detection method fails primarily due to the OCR model's inability to reliably detect digits. When digits are detected, the subsequent GP module performs as expected. Since the GP module will not be performed when the digits are not detected, the Digits Detection method being faster than RulerNet-GP despite using the same GP method is reasonable. One might argue that tuning the OCR model on a ruler dataset with digit location annotations could yield comparable performance to RulerNet. However, such tuning is more resource-intensive, as it requires annotations for all digits rather than simple point marks, and it is inherently less robust—while not all rulers contain digits, all rulers have marks. For the Mark Frequency method, the blue lines represent the most confident line along the ruler marks, and errors occur both during ruler localization and frequency estimation. These observations further support the design of RulerNet, where direct mark localization produces more robust and generalizable results.

#### E. Analysis of Failure Cases

Despite the strong robustness of RulerNet, there are still scenarios in which the model can become confused. We visualize several representative failure cases in Fig. 5. For instance, when ruler marks are not clearly visible (Row 1), RulerNet understandably fails to localize them. Transparent rulers placed against complex or cluttered backgrounds can also reduce mark visibility, as blending effects make it difficult for the model to distinguish the marks from the surroundings (Row 2). Additionally, objects or patterns that visually resemble centimeter markings (degree marks) may produce false positives (Row 3). In crowded scenes with multiple overlapping rulers, the model may struggle to disambiguate which marks belong to which ruler (Row 4).

To ensure accurate predictions in practice, users should consider the following recommendations:

- Use rulers with high-contrast markings that are clearly visible.
- Avoid transparent or reflective rulers in visually complex environments.
- Minimize background clutter near the ruler, especially textures or objects that resemble measurement marks.
- Ensure that the ruler lies flat and is not significantly occluded or distorted.
- If multiple rulers are present in a single frame, avoid overlapping when possible.

By following these guidelines, users can significantly reduce the likelihood of failure and help RulerNet achieve the most reliable scale estimation in real-world settings.

#### F. Ablation Study

In this subsection, we analyze the implications of our design choices and identify the components that contribute to a robust ruler reading model. All models were trained using the same architecture at an input resolution of  $768 \times 768$ , as larger training sizes would have incurred higher computational costs.

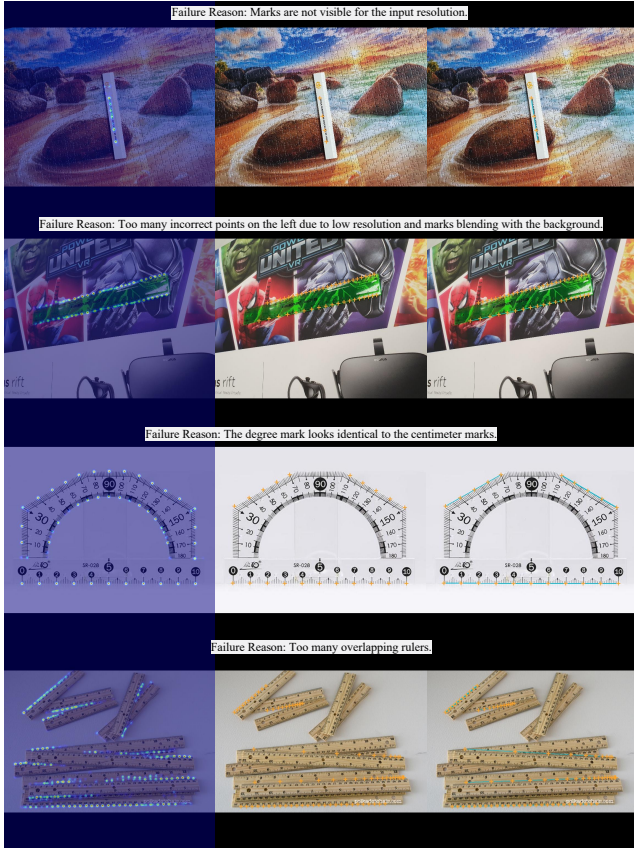


Fig. 5. Examples of failure cases from both the AnyRuler and Rulers2023 [26] datasets.

### Why did we prompt ControlNet with “rectangle” instead of “ruler”?

In our data generation pipeline, we deliberately used “rectangle” in the prompt instead of “ruler”. Even with ControlNet, it is difficult to isolate the location of specific features. If we directly prompted for a “ruler”, the model could have misinterpreted other parts of the image as rulers, leading to the generation of unintended marks. This phenomenon is akin to hallucinations observed in diffusion models [72]. As shown in Fig. 6, using “ruler” as the prompt can result in erroneous ruler marks. By contrast, only rulers generated from the graphics-based ruler generator included mark labels. Any unexpected marks generated in response to “ruler” would have been treated as background by the model, potentially degrading performance. Since our objective was to maintain full control over the ruler placement, we use the word “rectangle” instead of “ruler”.

### How did the ruler estimation method affect performance and speed?

To evaluate the impact of the ruler/scale estimation method on both performance and inference speed, we compared four different approaches:

- **Direct Adjacent Points:** Compute the distances between all adjacent points and take the average.
- **Median-based Filtering:** Compute the ratios between adjacent distances, retain only those within a 20% deviation from the median distance and a 10% deviation from

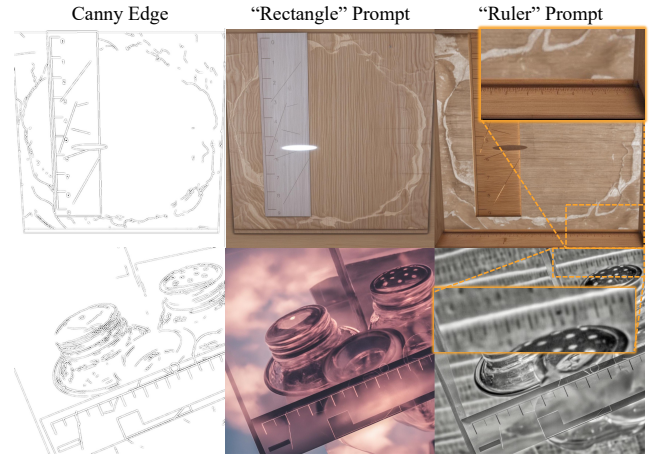


Fig. 6. Comparison of the prompt words “rectangle” and “ruler” in generated ruler images. The Canny edge maps are inverted for improved visualization.

TABLE III  
EVALUATION OF RULERNET WITH DIFFERENT SCALE ESTIMATION METHODS (MAPE/CM@768), TRAINED SOLELY ON THE ANYRULER DATASET. MILLISECONDS PER SIMPLE (MS/S) IS COMPUTED AS THE AVERAGE TIME IT TAKES TO EXTRACT THE RULER FROM THE PREDICTED MARKS ON ANYRULER DATASET.

	AnyRuler	Rulers2023 [26]	Avg.	ms/s
RulerNet-Direct	1.53	4.43	2.98	16.99
RulerNet-Median	1.33	3.65	2.49	16.08
RulerNet-GP	1.38	3.02	2.20	2497.33
RulerNet-DeepGP	0.84	2.78	1.81	22.61

the median ratio, and then average over the remaining distances.

- **GP Optimization Method:** Apply the proposed geometric progression (GP) optimization technique to estimate the entire ruler and compute the scale.
- **DeepGP:** Use the proposed DeepGP model to estimate the ruler’s GP parameters and compute the scale.

As shown in Table III, directly averaging adjacent point distances yielded the worst performance, highlighting the effect of noise in the detected points and the need for further post-processing. The median-based filtering method significantly improved accuracy on both datasets by mitigating the influence of outliers. Applying the GP optimization method resulted in further improvements, particularly on the Rulers2023 dataset. As illustrated in Fig. 7, this method not only recovered the full ruler but also corrected inaccurate detections, offering finer control over scale estimation.

More importantly, the proposed DeepGP model achieved additional performance gains across both datasets, suggesting that the training data generation strategy described in Algorithm 1 produced representative and diverse training samples. In addition to improved accuracy, DeepGP delivered over a 100× speedup in inference time compared to the optimization-based GP method, while maintaining comparable speed to other less generalizable approaches. This efficiency is achieved by leveraging GPU acceleration through a lightweight, feed-forward design.

### How did image resolution affect performance?



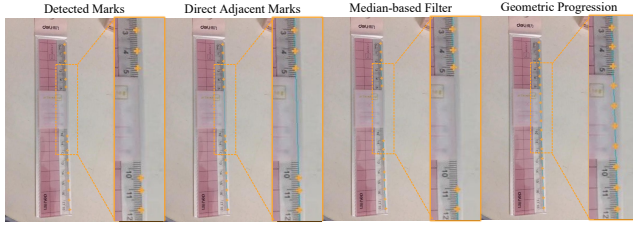


Fig. 7. Qualitative comparison of different ruler scale estimation methods. Images are zoomed in for improved visualization.

TABLE IV  
EVALUATION RULERNET-DIRECT ON DIFFERENT INFERENCE RESOLUTIONS (MAPE/CM@768). THE MODEL IS TRAINED SOLELY ON THE ANYRULER DATASET.

	AnyRuler	Rulers2023 [26]	Avg.
512	2.88	9.77	6.33
768	1.53	4.43	2.98
1,024	1.76	2.82	2.29
1,280	1.82	2.85	2.34

To study the effect of input image resolution on the model, we tested four different inference input resolutions using the baseline RulerNet trained on AnyRuler, with direct adjacent points distance used for scale estimation. Results were reported on both the AnyRuler and Rulers2023 testing sets.

As shown in Table IV, increasing resolution generally improved performance; however, beyond a certain point, further increases yielded diminishing returns. Notably, we observed performance degradation beginning at 1,024 on AnyRuler, while performance on Rulers2023 plateaued after 1,024. Further investigation revealed that AnyRuler images had a lower original resolution (an average of 1,036, with only 47% of images exceeding 768) compared to Rulers2023 (an average of 3,528, with all images exceeding 768). This suggests that AnyRuler may not benefit as much from higher input resolutions.

Additionally, we visualized the output heatmap at high and low resolutions, and for low-resolution images upsampled to high resolution (see Fig. 8). The observations indicate that when the original resolution is insufficient for the marks to be clearly visible (e.g., some images in the AnyRuler dataset), upsampling does not improve performance. This further supports our numerical findings.

#### How did the number of synthetic rulers per training epoch affect performance?

To study the effect of the number of synthetic rulers in each training epoch, in addition to using the AnyRuler dataset, we gradually increased the number of synthetic rulers up to 2,000 images until performance plateaued or began to decline. Since we have two types of synthetic rulers, we analyzed them in isolation; the combined effect is addressed later.

As shown in Table V, incorporating more synthetic rulers improved generalizability on the Rulers2023 dataset. Specifically, using generative images tends to enhance generalizability more than using graphics-based rulers. Although minor fluctuations in performance on the AnyRuler dataset were observed with generative rulers, the overall gains in gener-

Fig. 8. Qualitative example illustrating the effect of inference input resolution. Each column represents a different input resolution to the model. Each row represents a different original image resolution. Images are zoomed in for improved visualization.

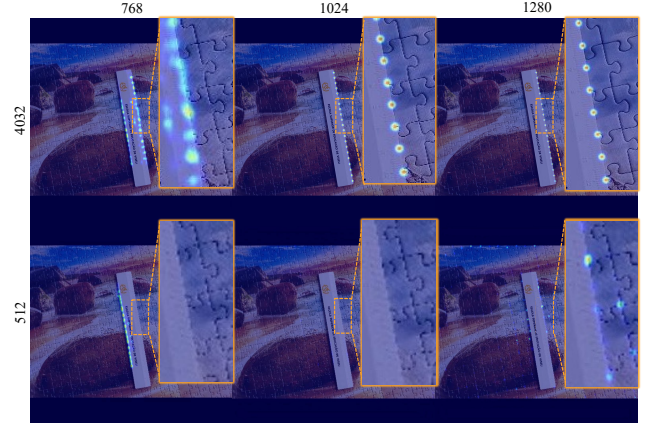


TABLE V  
EVALUATION ON DIFFERENT NUMBERS OF GRAPHICS-BASED RULERS OR GENERATIVE RULERS DURING TRAINING (MAPE/CM@768) USING THE DIRECT ADJACENT POINTS DISTANCE.

	Graphics-based		Generative	
	AnyRuler	Rulers2023 [26]	AnyRuler	Rulers2023 [26]
100	1.70	4.43	1.67	4.36
1,000	1.55	4.06	1.58	3.56
2,000	1.55	3.48	1.64	2.94

alization justified their increased use. Therefore, employing more generative synthetic rulers per training epoch led to a better-performing model.

#### How did the use of different synthetic ruler types affect performance?

We investigated how the combination of two different types of synthetic rulers affected model performance. First, we evaluated each type individually by training with 1,000 synthetic rulers from each method as a reference. Then, we evaluated the effect of using both types together during training.

As shown in Table VI, incorporating additional synthetic rulers improved performance on the Rulers2023 dataset. When combining both graphics-based and generative rulers, the improvement in generalizability on Rulers2023 was much greater than the slight performance degradation observed on AnyRuler, suggesting a potential trade-off between in-domain performance and generalizability. Based on results reported earlier, where adding more graphics-based rulers improved performance on both datasets, we argue that this perceived trade-off may result from insufficient training on a more diverse dataset. To test this hypothesis, we pre-trained the model using 102,000 generative synthetic rulers, 102,000 graphics-based rulers, and the AnyRuler training set before combining both types in the training phase. The number of synthetic rulers was chosen to balance performance and computational cost. This approach outperformed all previous configurations on both datasets. These results indicate that the additional use of synthetic rulers can greatly improve model performance, provided that the model is well trained.

TABLE VI

EVALUATION OF THE EFFECT OF COMBINING GRAPHICS-BASED (GRA.) AND GENERATIVE (GEN.) RULERS DURING TRAINING (MAPE/CM@768) USING THE DIRECT ADJACENT POINTS DISTANCE. “PRE.” INDICATES PRE-TRAINING THE MODEL WITH A LARGE NUMBER OF GRAPHICS-BASED AND GENERATIVE RULERS.

	AnyRuler	Rulers2023 [26]
RulerNet	1.53	4.43
+ Gra.	1.55	4.06
+ Gen.	1.58	3.56
+ Gen. + Gra.	1.61	2.87
+ Gen. + Gra. + Pre.	1.50	1.82

By answering the above questions, we further validate the effectiveness of the proposed data generation pipeline, model training strategy, and post-processing method. With proper settings, RulerNet achieves excellent performance.

## V. LIMITATIONS AND FUTURE DIRECTIONS

Although RulerNet achieves state-of-the-art performance and robustness for ruler reading in the wild, several limitations constrain its current scope and point to avenues for future research.

- **Planarity and flexibility:** The present formulation assumes straight, rigid rulers subject to perspective distortion, as encoded by the GP. Consequently, flexible or highly deformed measuring tools, e.g., soft measuring tapes, lie outside the model’s field of view. Camera pre-calibration can mitigate global effects such as radial lens distortion [73], yet broader deployment will require explicit modeling of non-planar rulers or adaptive distortion compensation.
- **2D-to-3D generalization:** RulerNet estimates scale solely in the image plane and preassumes that both ruler and target object lie on (or near) the same physical plane. Extending to full 3D measurement would demand reliable depth reconstruction between ruler and object, for instance via monocular relative-depth estimation. The absence of benchmark datasets that contain aligned 3D ground truth together with ruler context—as ruler-annotated RGB-D scenes are extremely rare—makes both algorithm design and rigorous evaluation non-trivial.
- **Out-of-plane distortion:** While the GP module captures perspective along the ruler’s longitudinal axis, distortions orthogonal to that axis remain unmodeled. Objects offset from the ruler plane therefore incur scale errors. Possible remedies include multi-ruler triangulation, fusion with inertial cues (e.g., leveraging smartphone gyroscope data for homography compensation and camera pose compensation [74]), or post-capture geometric rectification.
- **Ruler-mark detection robustness:** Both the Hough transform and GP stages rely on accurate detection of ruler marks. Severe occlusion, blur, or atypical markings degrade performance and may necessitate manual intervention. Future work could incorporate a learned verification or uncertainty estimation mechanism to identify and filter low-confidence detections and trigger user guidance,

thereby increasing reliability in challenging real-world settings.

## VI. CONCLUSION

In this work, we introduced RulerNet, a novel framework for robust ruler reading that integrates deep learning with geometric reasoning to enable accurate scale estimation in the wild. Our method contributes three core technical innovations: (1) a distortion-invariant keypoint detection framework that supports training on diverse and imperfect ruler data; (2) a geometric progression-based formulation for metric scale inference, capable of handling perspective distortions; and (3) DeepGP, a lightweight, feed-forward network that accelerates inference while remaining resilient to noisy detections. These innovations extend beyond ruler reading and offer general solutions for metric reasoning under projective distortion.

More broadly, this work demonstrates how AI-driven measurement systems can bridge the gap between digital perception and physical dimensions. In addition to meeting our internal needs as part of the PlacentaVision project—where accurate measurements support morphological characterization of the placenta [15] and clinical assessment of maternal and neonatal health [75]—our method addresses the growing demand for scalable and adaptable measurement tools in fields such as augmented reality, robotics, cataloging, and medical diagnostics. RulerNet offers a practical and extensible blueprint for integrating scale estimation with segmentation and scene understanding methods. By minimizing the need for manual annotations and leveraging both graphics- and diffusion-based synthetic data, RulerNet paves the way for the next generation of AI-assisted measurement tools—systems that are not only accurate, but also generalizable, efficient, and ready for deployment in real-world scenarios.

## REFERENCES

- [1] A. Kresha, “Trismus... gnashing of the teeth,” <https://www.emdocs.net/trismus-gnashing-of-the-teeth/>, Aug 2019.
- [2] <https://www.cancer.org/cancer/types/skin-cancer/skin-cancer-image-gallery.html>.
- [3] <https://www.crimemuseum.org/crime-library/forensic-investigation/footprints/>, Aug 2023.
- [4] <https://www.ebay.com/itm/112733250366>.
- [5] <https://dep.nj.gov/njfw/fishing/marine/delaware-bay-finish-trawl-survey/>.
- [6] S. Minaee, Y. Boykov, F. Porikli, A. Plaza, N. Kehtarnavaz, and D. Terzopoulos, “Image segmentation using deep learning: A survey,” *IEEE Transactions on Pattern Analysis and Machine Intelligence*, vol. 44, no. 7, pp. 3523–3542, 2021.
- [7] K. Grauman, A. Westbury, E. Byrne, Z. Chavis, A. Furnari, R. Girdhar, J. Hamburger, H. Jiang, M. Liu, X. Liu *et al.*, “Ego4D: Around the world in 3,000 hours of egocentric video,” in *Proceedings of the IEEE/CVF Conference on Computer Vision and Pattern Recognition*, 2022, pp. 18995–19012.
- [8] N. R. Abbasi, M. Yancovitz, D. Gutkowitz-Krusin, K. S. Panageas, M. C. Mihm, P. Googe, R. King, V. Prieto, I. Osman, R. J. Friedman *et al.*, “Utility of lesion diameter in the clinical diagnosis of cutaneous melanoma,” *Archives of Dermatology*, vol. 144, no. 4, pp. 469–474, 2008.
- [9] D. J. Thomas, A. R. King, and B. G. Peat, “Excision margins for nonmelanotic skin cancer,” *Plastic and Reconstructive Surgery*, vol. 112, no. 1, pp. 57–63, 2003.
- [10] N. Kaessli, R. Guigourès, and R. Shirvany, “SizeNet: Weakly supervised learning of visual size and fit in fashion images,” in *Proceedings of the IEEE/CVF Conference on Computer Vision and Pattern Recognition Workshops*, 2019, pp. 0–0.



- [11] Y. Eshel, O. Levi, H. Roitman, and A. Nus, "PreSize: predicting size in e-commerce using transformers," in *Proceedings of the 44th International ACM SIGIR Conference on Research and Development in Information Retrieval*, 2021, pp. 255–264.
- [12] O. Chatterjee, J. R. Tej, and N. V. Dasaraju, "Incorporating customer reviews in size and fit recommendation systems for fashion e-commerce," *arXiv preprint arXiv:2208.06261*, 2022.
- [13] Q. Zhang, C. He, W. Qin, D. Liu, J. Yin, Z. Long, H. He, H. C. Sun, and H. Xu, "Eliminate the hardware: Mobile terminals-oriented food recognition and weight estimation system," *Frontiers in Nutrition*, vol. 9, p. 965801, 2022.
- [14] F. S. Konstantakopoulos, E. I. Georga, and D. I. Fotiadis, "A novel approach to estimate the weight of food items based on features extracted from an image using boosting algorithms," *Scientific Reports*, vol. 13, no. 1, p. 21040, 2023.
- [15] Y. Chen, Z. Zhang, C. Wu, D. Davaasuren, J. A. Goldstein, A. D. Gernand, and J. Z. Wang, "AI-PLAX: AI-based placental assessment and examination using photos," *Computerized Medical Imaging and Graphics*, vol. 84, p. 101744, 2020.
- [16] H. Mirzaalian Dastjerdi, D. Töpfer, S. J. Rupitsch, and A. Maier, "Measuring surface area of skin lesions with 2D and 3D algorithms," *International Journal of Biomedical Imaging*, vol. 2019, no. 1, p. 4035148, 2019.
- [17] Y.-T. Lin, Y.-C. Lin, and J.-Y. Han, "Automatic water-level detection using single-camera images with varied poses," *Measurement*, vol. 127, pp. 167–174, 2018.
- [18] J. An, K. Song, D. Wu, and W. He, "A water level ruler recognition method based on deep learning technology," in *Proceedings of the International Conference on Intelligent Computing*. Springer, 2023, pp. 40–50.
- [19] X. Yan, Q. Pan, and Y. Zhao, "Soil profile ruler detection in YOLOv5," in *Proceedings of the International Conference on Generative Artificial Intelligence and Information Security*, 2024, pp. 324–328.
- [20] I. Gertsovich, M. Nilsson, J. Bartůňek, and I. Claesson, "Automatic estimation of a scale resolution in forensic images," *Forensic Science International*, vol. 283, pp. 58–71, 2018.
- [21] Z. Wen, R. M. Smith, M. Connor, and J. Curran, "A ruler detection method for auto-adjusting scales of shoeprint images," *Science & Justice*, vol. 64, no. 5, pp. 498–508, 2024.
- [22] A. Hurst, A. Lerer, A. P. Goucher, A. Perelman, A. Ramesh, A. Clark, A. Ostrow, A. Welihinda, A. Hayes, A. Radford *et al.*, "Gpt-4o system card," *arXiv preprint arXiv:2410.21276*, 2024.
- [23] S. Jun, "Research on image measuring method based on monocular camera and ruler," in *Proceedings of the Conference on Informatization in Education, Management and Business*. Atlantis Press, 2015, pp. 150–155.
- [24] M. Telahun, D. Sierra-Sossa, and A. S. Elmaghraby, "Heuristic analysis for in-plane non-contact calibration of rulers using mask R-CNN," *Information*, vol. 11, no. 5, p. 259, 2020.
- [25] B. Lukashchuk, "Method of automatic identification of ruler scales on images to solve the problem of estimating the geometric dimensions of certain objects," in *Proceedings of the IEEE 3rd KhPI Week on Advanced Technology*. IEEE, 2022, pp. 1–4.
- [26] D. Matuzevičius, "An annotated dataset of synthetic and real images for ruler detection using deep learning," *Electronics*, vol. 12, no. 24, p. 4924, 2023.
- [27] D. A. Kononov, J. A. Domingos, C. Bajema, R. D. White, and D. R. Jerry, "Ruler detection for automatic scaling of fish images," in *Proceedings of the International Conference on Advances in Image Processing*, 2017, pp. 90–95.
- [28] A. Bhalerao and G. Reynolds, "Ruler detection for autoscaling forensic images," *International Journal of Digital Crime and Forensics*, vol. 6, no. 1, pp. 9–27, 2014.
- [29] M. Herrmann, S. Zambanini, and M. Kampel, "Image-based measurement of ancient coins," in *Proceedings of the International Conference on Computer Applications and Quantitative Methods in Archaeology*. Oxford: Archaeopress, 2010.
- [30] Z. Zhang, Y. Zhou, H. Liu, and H. Gao, "In-situ water level measurement using nir-imaging video camera," *Flow Measurement and Instrumentation*, vol. 67, pp. 95–106, 2019.
- [31] G. Chen, K. Bai, Z. Lin, X. Liao, S. Liu, Z. Lin, Q. Zhang, and X. Jia, "Method on water level ruler reading recognition based on image processing," *Signal, Image and Video Processing*, vol. 15, pp. 33–41, 2021.
- [32] G. Bai, J. Hou, Y. Zhang, B. Li, H. Han, T. Wang, R. Hinkelmann, D. Zhang, and L. Guo, "An intelligent water level monitoring method based on SSD algorithm," *Measurement*, vol. 185, p. 110047, 2021.
- [33] G. Dou, R. Chen, C. Han, Z. Liu, and J. Liu, "Research on water-level recognition method based on image processing and convolutional neural networks," *Water*, vol. 14, no. 12, p. 1890, 2022.
- [34] R. Qiu, Z. Cai, Z. Chang, S. Liu, and G. Tu, "A two-stage image process for water level recognition via dual-attention CornerNet and CTransformer," *The Visual Computer*, vol. 39, no. 7, pp. 2933–2952, 2023.
- [35] S. Liu, W. Zheng, X. Wang, H. Xiong, J. Cheng, C. Yong, W. Zhang, and X. Zou, "A novel depth measurement method for urban flooding based on surveillance video images and a floating ruler," *Natural Hazards*, vol. 119, no. 3, pp. 1967–1989, 2023.
- [36] A. Gooßen, M. Schlüter, M. Hensel, T. Pralow, and R.-R. Grigat, "Ruler-based automatic stitching of spatially overlapping radiographs," in *Bildverarbeitung für die Medizin 2008: Algorithmen—Systeme—Anwendungen Proceedings des Workshops vom 6. bis 8. April 2008 in Berlin*. Springer, 2008, pp. 192–196.
- [37] C. Chen, R. Kojcev, D. Haschtmann, T. Fekete, L. Nolte, and G. Zheng, "Ruler based automatic C-arm image stitching without overlapping constraint," *Journal of Digital Imaging*, vol. 28, pp. 474–480, 2015.
- [38] Z. Xue, K. Yu, P. Pearlman, T.-C. Chen, C.-H. Hua, C. J. Kang, C.-Y. Chien, M.-H. Tsai, C.-P. Wang, A. Chaturvedi *et al.*, "Extraction of ruler markings for estimating physical size of oral lesions," in *Proceedings of the International Conference on Pattern Recognition*. IEEE, 2022, pp. 4241–4247.
- [39] Z. Xue, K. Yu, P. C. Pearlman, A. Pal, T.-C. Chen, C.-H. Hua, C. J. Kang, C.-Y. Chien, M.-H. Tsai, C.-P. Wang *et al.*, "Automatic detection of oral lesion measurement ruler toward computer-aided image-based oral cancer screening," in *Proceedings of the Annual International Conference of the IEEE Engineering in Medicine & Biology Society*. IEEE, 2022, pp. 3218–3221.
- [40] A. Bauer, S. Trapp, M. Stenger, R. Leppich, S. Kounev, M. Leznik, K. Chard, and I. Foster, "Comprehensive exploration of synthetic data generation: A survey," *arXiv preprint arXiv:2401.02524*, 2024.
- [41] G. Ros, L. Sellart, J. Materzynska, D. Vazquez, and A. M. Lopez, "The synthia dataset: A large collection of synthetic images for semantic segmentation of urban scenes," in *Proceedings of the IEEE Conference on Computer Vision and Pattern Recognition*, 2016, pp. 3234–3243.
- [42] A. Gaidon, Q. Wang, Y. Cabon, and E. Vig, "Virtual worlds as proxy for multi-object tracking analysis," in *Proceedings of the IEEE Conference on Computer Vision and Pattern Recognition*, 2016, pp. 4340–4349.
- [43] S. R. Richter, V. Vineet, S. Roth, and V. Koltun, "Playing for data: Ground truth from computer games," in *Proceedings of the European Conference on Computer Vision*. Springer, 2016, pp. 102–118.
- [44] D. Matuzevičius, A. Serackis, and D. Navakauskas, "Mathematical models of oversaturated protein spots," *Elektronika ir elektrotechnika*, vol. 73, no. 1, pp. 63–68, 2007.
- [45] M. Peris, S. Martull, A. Maki, Y. Ohkawa, and K. Fukui, "Towards a simulation driven stereo vision system," in *Proceedings of the International Conference on Pattern Recognition*. IEEE, 2012, pp. 1038–1042.
- [46] K. Rematas, T. Ritschel, M. Fritz, and T. Tuytelaars, "Image-based synthesis and re-synthesis of viewpoints guided by 3D models," in *Proceedings of the IEEE Conference on Computer Vision and Pattern Recognition*, 2014, pp. 3898–3905.
- [47] J. Papon and M. Schoeler, "Semantic pose using deep networks trained on synthetic RGB-D," in *Proceedings of the IEEE International Conference on Computer Vision*, 2015, pp. 774–782.
- [48] X. Li, K. Wang, X. Gu, F. Deng, and F.-Y. Wang, "Paralleleye pipeline: An effective method to synthesize images for improving the visual intelligence of intelligent vehicles," *IEEE Transactions on Systems, Man, and Cybernetics: Systems*, vol. 53, no. 9, pp. 5545–5556, 2023.
- [49] A. Antoniou, "Data augmentation generative adversarial networks," *arXiv preprint arXiv:1711.04340*, 2017.
- [50] X. Zhu, Y. Liu, Z. Qin, and J. Li, "Data augmentation in emotion classification using generative adversarial networks," *arXiv preprint arXiv:1711.00648*, 2017.
- [51] C. Bowles, L. Chen, R. Guerrero, P. Bentley, R. Gunn, A. Hammers, D. A. Dickie, M. V. Hernández, J. Wardlaw, and D. Rueckert, "GAM augmentation: Augmenting training data using generative adversarial networks," *arXiv preprint arXiv:1810.10863*, 2018.
- [52] H.-C. Shin, N. A. Tenenholtz, J. K. Rogers, C. G. Schwarz, M. L. Senjem, J. L. Gunter, K. P. Andriole, and M. Michalski, "Medical image synthesis for data augmentation and anonymization using generative adversarial networks," in *Proceedings of the Third International Workshop on Simulation and Synthesis in Medical Imaging, held in conjunction with the 21st International Conference on Medical Image Computing and Computer-Assisted Intervention*. Springer, 2018, pp. 1–11.

- [53] X. Zhu, Y. Liu, J. Li, T. Wan, and Z. Qin, "Emotion classification with data augmentation using generative adversarial networks," in *Proceedings of the Advances in Knowledge Discovery and Data Mining*. Springer, 2018, pp. 349–360.
- [54] O. Bailo, D. Ham, and Y. Min Shin, "Red blood cell image generation for data augmentation using conditional generative adversarial networks," in *Proceedings of the IEEE/CVF Conference on Computer Vision and Pattern Recognition Workshops*, 2019, pp. 0–0.
- [55] V. Sandfort, K. Yan, P. J. Pickhardt, and R. M. Summers, "Data augmentation using generative adversarial networks (CycleGAN) to improve generalizability in ct segmentation tasks," *Scientific Reports*, vol. 9, no. 1, p. 16884, 2019.
- [56] S. Motamed, P. Rogalla, and F. Khalvati, "Data augmentation using generative adversarial networks (GANs) for GAN-based detection of pneumonia and covid-19 in chest x-ray images," *Informatics in Medicine Unlocked*, vol. 27, p. 100779, 2021.
- [57] B. Trabucco, K. Doherty, M. Gurinas, and R. Salakhutdinov, "Effective data augmentation with diffusion models," *arXiv preprint arXiv:2302.07944*, 2023.
- [58] C.-M. Feng, K. Yu, Y. Liu, S. Khan, and W. Zuo, "Diverse data augmentation with diffusions for effective test-time prompt tuning," in *Proceedings of the IEEE/CVF International Conference on Computer Vision*, 2023, pp. 2704–2714.
- [59] X. Zhang, A. Gangopadhyay, H.-M. Chang, and R. Soni, "Diffusion model-based data augmentation for lung ultrasound classification with limited data," in *Proceedings of the Machine Learning for Health Workshop at the Conference on Neural Information Processing Systems*, 2023, pp. 664–676.
- [60] D. Chen, X. Qi, Y. Zheng, Y. Lu, Y. Huang, and Z. Li, "Synthetic data augmentation by diffusion probabilistic models to enhance weed recognition," *Computers and Electronics in Agriculture*, vol. 216, p. 108517, 2024.
- [61] H. Fang, B. Han, S. Zhang, S. Zhou, C. Hu, and W.-M. Ye, "Data augmentation for object detection via controllable diffusion models," in *Proceedings of the IEEE/CVF Winter Conference on Applications of Computer Vision*, 2024, pp. 1257–1266.
- [62] Y. Fu, C. Chen, Y. Qiao, and Y. Yu, "DreamDA: Generative data augmentation with diffusion models," *arXiv preprint arXiv:2403.12803*, 2024.
- [63] K. Islam, M. Z. Zaheer, A. Mahmood, and K. Nandakumar, "DiffuseMix: Label-preserving data augmentation with diffusion models," in *Proceedings of the IEEE/CVF Conference on Computer Vision and Pattern Recognition*, 2024, pp. 27 621–27 630.
- [64] P. Alimisis, I. Mademlis, P. Radoglou-Grammatikis, P. Sarigiannidis, and G. T. Papadopoulos, "Advances in diffusion models for image data augmentation: A review of methods, models, evaluation metrics and future research directions," *arXiv preprint arXiv:2407.04103*, 2024.
- [65] J. Wang, K. Sun, T. Cheng, B. Jiang, C. Deng, Y. Zhao, D. Liu, Y. Mu, M. Tan, X. Wang *et al.*, "Deep high-resolution representation learning for visual recognition," *IEEE Transactions on Pattern Analysis and Machine Intelligence*, vol. 43, no. 10, pp. 3349–3364, 2020.
- [66] J. Deng, W. Dong, R. Socher, L.-J. Li, K. Li, and L. Fei-Fei, "ImageNet: A large-scale hierarchical image database," in *Proceedings of the IEEE Conference on Computer Vision and Pattern Recognition*. IEEE, 2009, pp. 248–255.
- [67] L. Zhang, A. Rao, and M. Agrawala, "Adding conditional control to text-to-image diffusion models," in *Proceedings of the IEEE/CVF International Conference on Computer Vision*, 2023, pp. 3836–3847.
- [68] A. Bakshi, P. Indyk, R. Jayaram, S. Silwal, and E. Waingarten, "Near-linear time algorithm for the chamfer distance," *Advances in Neural Information Processing Systems*, vol. 36, pp. 66 833–66 844, 2023.
- [69] R. Storn and K. Price, "Differential evolution—a simple and efficient heuristic for global optimization over continuous spaces," *Journal of Global Optimization*, vol. 11, pp. 341–359, 1997.
- [70] D. Qin, C. Lechner, M. Delakis, M. Fornoni, S. Luo, F. Yang, W. Wang, C. Banbury, C. Ye, B. Akin *et al.*, "Mobilenetv4: universal models for the mobile ecosystem," in *Proceedings of the European Conference on Computer Vision*. Springer, 2024, pp. 78–96.
- [71] O. Ronneberger, P. Fischer, and T. Brox, "U-net: Convolutional networks for biomedical image segmentation," in *Proceedings of the Medical Image Computing and Computer-Assisted Intervention*. Springer, 2015, pp. 234–241.
- [72] S. K. Aithal, P. Maini, Z. Lipton, and J. Z. Kolter, "Understanding hallucinations in diffusion models through mode interpolation," *Advances in Neural Information Processing Systems*, vol. 37, pp. 134 614–134 644, 2025.
- [73] Z. Zhang, Y. Matsushita, and Y. Ma, "Camera calibration with lens distortion from low-rank textures," in *CVPR 2011*. IEEE, 2011, pp. 2321–2328.
- [74] H. Li, K. Luo, B. Zeng, and S. Liu, "Gyroflow+: Gyroscope-guided unsupervised deep homography and optical flow learning," *International Journal of Computer Vision*, vol. 132, no. 6, pp. 2331–2349, 2024.
- [75] Y. Pan, M. Mehta, J. A. Goldstein, J. Ngonzi, L. M. Bebell, D. J. Roberts, C. K. Carreon, K. Gallagher, R. E. Walker, A. D. Gernand *et al.*, "Cross-modal contrastive learning for unified placenta analysis using photographs," *Patterns*, vol. 5, no. 12, 2024.



**Yimu Pan** is a Ph.D. candidate in the Informatics program at The Pennsylvania State University, advised by James Z. Wang. His research centers around the fields of computer vision and machine learning, with a specific emphasis on vision-language techniques and medical image applications. Before starting his Ph.D. program, he received bachelor's degrees in Computer Science, Mathematics, and Statistics from The Pennsylvania State University.



**Manas Mehta** is a Ph.D. student in the College of Information Sciences and Technology at The Pennsylvania State University, advised by James Z. Wang. His research focuses on computer vision and deep learning, with applications in medical imaging and socially responsible AI. Prior to joining Penn State, they earned both their B.S. and M.S. degrees in Computer Science from Worcester Polytechnic Institute, where they were advised by Jacob Whitehill and Lane Harrison.



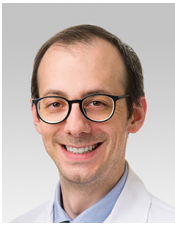
biology emphasis from the University of Idaho.

**Gwen Sincerbeaux** is a graduate student in the Department of Nutritional Sciences at The Pennsylvania State University, advised by Alison Z. Gernand in the Micronutrients and Pregnancy Lab (MAP). Her research focuses on maternal and child health, with particular interests in micronutrients, mineral and transition metal metabolism, biomarker discovery, and the integration of deep learning techniques in nutritional science. She holds a Master of Science in Bioinformatics from Johns Hopkins University and a Bachelor of Science in Mathematics with a



low-cost methods to make assessments of the placenta and plasma volume expansion. Her ongoing work leading a large, international collaborative team is developing PlacentaVision, an AI-based software to assess placentas via digital photograph.

**Alison D. Gernand** is an Associate Professor in the Department of Nutritional Sciences at The Pennsylvania State University. She completed her PhD in international health and human nutrition at the Johns Hopkins Bloomberg School of Public Health and her postdoctoral training in nutritional epidemiology at the University of Pittsburgh School of Public Health. Her research is focused on maternal nutritional status and adverse pregnancy outcomes in low- and middle-income countries. Work in low-resource settings has led her to develop and validate simple,



**Jeffery A. Goldstein** is the Director of Perinatal Pathology in the Department of Pathology at Northwestern Memorial Hospital, Northwestern University, Chicago. His long-term goal is to build highly collaborative groups to improve maternal-child health using AI in the placenta. He completed an MD and PhD at the University of Chicago. He completed a residency and fellowship in Anatomic and Pediatric Pathology, with ongoing clinical work in placental pathology. He has worked successfully with teams at the interface of clinical medicine and

translational science, as in his work with the AI-PLAX rapid placental diagnostics project, the SNIPP study of COVID-19, and AI identification of gestational age, macroscopic placental lesions, and prostate cancer.



**James Z. Wang** (Senior Member, IEEE) is a Distinguished Professor of the Data Sciences and Artificial Intelligence section of the College of Information Sciences and Technology at The Pennsylvania State University. He received the bachelor's degree in mathematics *summa cum laude* from the University of Minnesota (1994), and the MS degree in mathematics (1997), the MS degree in computer science (1997), and the PhD degree in medical information sciences (2000), all from Stanford University. His research interests include image analysis, affective

computing, image modeling, image retrieval, and their applications. He was a visiting professor at the Robotics Institute at Carnegie Mellon University (2007-2008), a lead special section guest editor of the IEEE Transactions on Pattern Analysis and Machine Intelligence (2008), a program manager at the Office of the Director of the National Science Foundation (2011-2012), and a special issue guest editor of the IEEE BITS – The Information Theory Magazine (2022). He was also affiliated with the Department of Communication and Media, School of Social Sciences and Humanities, Loughborough University, UK (2023-2024). He was a recipient of a National Science Foundation Career Award (2004) and Amazon Research Awards (2018-2022).